Available online at www.sciencedirect.com
SCIENCE DIRECT
Thin Solid Films 473 (2005) 89–97
thin solid films
www.elsevier.com/locate/tsf

Chemical, optical, vibrational and luminescent properties of hydrogenated silicon-rich oxynitride films

Sandeep Kohli[a,*], Jeremy A. Theil[b], Patricia C. Dippo[c], Richard K. Ahrenkiel[c], Christopher D. Rithner[a], Peter K. Dorhout[a]

[a]*Department of Chemistry, Colorado State University, Fort Collins, CO 80523, USA*
[b]*Agilent Technologies, MS 51L-GW, 5301 Stevens Creek Boulevard, Santa Clara, CA 95051, USA*
[c]*Measurements and Characterization Division, National Renewable Energy Laboratory, 1617 Cole Boulevard, Golden, CO 80401, USA*

Received 4 November 2003; received in revised form 12 July 2004; accepted 14 July 2004
Available online 26 August 2004

Abstract

X-ray photoelectron spectroscopy, spectroscopic ellipsometry, Fourier transform infrared and room temperature photoluminescence spectroscopy has been used to investigate the chemical, optical, vibrational and luminescent properties of Plasma Enhanced Chemical Vapor Deposited SiO_xN_y/H ($0.17 \le x \le 0.96$; $0.07 \le y \le 0.27$), hydrogenated silicon-rich oxynitride (SRON). The linear dependence of the refractive index of the SRON films on the O/Si ratio was established. The photoluminescence from the SRON films were attributed to the embedded amorphous silicon clusters in the films. The dependence of luminescence maximum values on the O/Si and O/N ratios has been explored. We postulate that at O/Si ratio of 0.18 and an O/N ratio of 2.0 ($SiO_{0.18}N_{0.09}$) the film underwent a transformation from silicon-rich oxynitride to a-Si/H film with oxygen and nitrogen impurities.

PACS: 78.20.Ci; 78.30.−jl; 79.60.−i
Keywords: Silicon-rich silicon oxynitride; XPS; Ellipsometry; Photoluminescence; Thin film

1. Introduction

Amorphous silicon-oxynitride thin films can have a refractive index varying from 2.0 to 1.46 (at 635 nm) and a dielectric constant in the range of 7.5–3.9 eV depending upon the nitrogen content [1]. The large variation of the refractive index is among the most interesting properties of silicon oxynitride (SiO_xN_y) films, enabling the design of a large variety of waveguide structures [2]. Silicon oxynitride films effectively retard dopant diffusion through the gate dielectric that may degrade the performance of a metal-oxide-semiconductor field effect transistor [3]. Hence, Si–O–N films are among the leading candidates to replace SiO_2 for sub-0.13-μm technology that requires a SiO_2 film thickness below 2 nm [1,3]. The materials properties pertaining to the integrity and reliability of these Si–O–N films have been described in recent review articles [1,2,4].

Photoluminescence (PL) [5] and electroluminescence [6] properties of hydrogenated Si–O–N films have been studied in the past. While the presence of defects in the silicon-suboxide was speculated to provide radiative centers for room temperature PL [5], electroluminescence was considered to be caused by the electronic transitions between band-tail states related to silicon–nitrogen bonds [6]. However, the visible PL at room temperature in silicon-rich oxynitride films has been attributed to the presence of amorphous silicon clusters in the film [7].

The aim of the present work is to investigate the dependence of the chemical, optical and vibrational properties of low temperature plasma enhanced chemical vapor deposited [8] SiO_xN_y/H ($0.17 \le x \le 0.96$; $0.07 \le y \le 0.27$) films

* Corresponding author. Tel.: +1 970 491 4076; fax: +1 970 491 1801.
E-mail address: skohli@lamar.colostate.edu (S. Kohli).

0040-6090/$ - see front matter © 2004 Elsevier B.V. All rights reserved.
doi:10.1016/j.tsf.2004.07.054

on the silicon content of the films. Glancing Angle X-ray Diffraction (GAXRD), X-ray Photoelectron Spectroscopy (XPS), Spectroscopic Ellipsometry, Fourier Transform Infrared (FTIR) spectroscopy and room temperature PL measurements have been used to characterize the samples. Of importance here are the studies aimed at investigating the chemical, optical, vibrational and luminescence properties of hydrogenated silicon-rich oxynitride films with extremely high silicon contents. The increased silicon content, particularly when O/Si ratio drops below 0.5, is likely to have limiting effects on these properties of the films.

2. Experimental details

Hydrogenated silicon-rich oxynitride (SRON) films, in the composition range SiO_xN_y/H ($0.17 \le x \le 0.96$; $0.07 \le y \le 0.27$), were deposited on Si(100) wafers with a 500-nm SiO_2 interlayer using low temperature plasma enhanced chemical vapor deposition process [8].

A Bruker D-8 Discover X-ray diffraction system with a Cu X-ray source and line focus optics was used in the GAXRD measurements. A Göbel mirror was placed on the primary beam side to achieve monochromatic and parallel X-ray beams in the laboratory [9,10]. A scintillation detector and soller slits (~0.4° separation) were used on the diffracted beam side to record the XRD spectra. GAXRD measurements were performed with a fixed angle of incidence of 0.5° to maximize the signal from the films and a detector scan was carried out to record the diffracted X-ray intensity as a function of 2θ.

XPS measurements were performed using a Physical Electronics Model 5800 spectrometer. Monochromatic $Al_{K\alpha}$ energy, 1486.6 eV, was employed as an X-ray source. The collection angle for all the measurements was 45°. An initial survey scan (pass energy 93.9 eV, step size 0.8 eV) was done to determine the elemental composition. Integrated peak intensities under O 1s, Si 2p, N 1s and C 1s peaks were used for estimating the relative elemental compositions of the films. The integrated peak area was normalized with respect to each core level atomic sensitivity factor [11]. Scans for chemical state identification of the elements were carried out with pass energy of 23.5 eV and a step size of 0.1 eV. The samples were sputtered with Ar^+ to remove the surface contaminants. XPSPEAK Version 4.1 peak fitting software was used to deconvolute individual peak components. Peaks were fitted using the Gaussian–Lorentzian peak profile and a Shirley background was used. Some adventitious carbon, intentionally left on the film surface, was used to determine the offset of the binding energy (BE) of the C 1s peak (385 eV) [12] induced due to the surface charging effects. The binding energy of elemental Si $2p_{3/2}$, reported in literature, is 99.79 eV [12] and was used to fine correct the peak shift due to the charging effects for samples with elemental silicon components.

The Si 2p peak for elemental silicon comprises the Si $2p_{3/2}$ and Si $2p_{1/2}$ doublet, separated in energy by 0.6 eV and having an area ratio ($A_{Si\ 2p1/2}/A_{Si\ 2p3/2}$) of 0.5 [13,14]. The full width half maxima (FWHM) of elemental Si $2p_{1/2}$ and Si $2p_{3/2}$ were fixed at the values of FWHM of an Ar^+ sputtered Si(100) substrate. For our apparatus, Si $2p_{3/2}$ FWHM values of Ar^+ etched and chemically etched Si(100) substrates were found to be 0.85 and 0.68 eV, respectively. The Si 2p FWHM value for stiochiometric SiO_2 (Si^{4+}) under similar conditions was found to be 1.8 eV and was fixed for the peak fit procedure. The FWHM for silicon sub-oxides (Si^{1+}–Si^{3+}) were varied between 1.1 and 1.5 eV. The FWHM of the N 1s peaks for nitrides typically lie between 0.9 and 1.1 eV. All these constraints were used to fit the Si 2p and N 1s XPS spectra of the films.

Variable angle spectroscopic ellipsometry data for SRON films were acquired using J.A. Woollam ellipsometer at a fixed wavelength (λ) of 600 nm as the angle of incidence varied from 15° to 85° in steps of 1°. Optical modeling and data analysis were done using the WVASE32 software package [15]. Ellipsometric data ψ and Δ for multiple angles were fitted in the optical models. The SRON films were fitted using the Bruggemann Effective Medium Approximation [15] model assuming the film to be composed of Si and SiO_2. A 500-nm SiO_2 interlayer, whose optical constants were obtained separately by fitting the ellipsometric data, was included between the Effective Medium Approximation model layer and the Si substrate in our model.

FTIR transmission measurements in the spectral range 450–4000 cm^{-1} were carried out using a Thermo Nicolet MagnaIR 760 spectrophotometer equipped with a deuterated triglycine sulfate detector with KBr windows and an XT-KBr beam splitter. The spectral resolution for the measurements was 4 cm^{-1}. The sample compartment was purged with nitrogen. For all the spectra, a 500-nm SiO_2 film deposited on a Si wafer was used as a background to isolate the peaks related to the SRON layers.

The PL data were taken using the Oriel InstaSpec IV Charged Coupled Device and the MS-257 Imaging Spectrograph, with the InstaSpec data acquisition software. The data was corrected for system response, neutral density filters, and long pass filters. The laser used for excitation was a Kimmon IK Series 442 nm He–Cd laser at 20 mW. An interference filter was used to pass only the laser line.

3. Results

A lack of crystalline features in the GAXRD pattern indicated that the as-deposited SRON films were amorphous over the entire composition range investigated. A survey XPS spectrum taken after the sputter removal of surface contaminants showed that the compositions of the five films prepared were $SiO_{0.96}N_{0.27}$, $SiO_{0.49}N_{0.19}$, $SiO_{0.29}N_{0.13}$, $SiO_{0.18}N_{0.09}$, and $SiO_{0.17}N_{0.07}$.

The measured and fitted high-resolution Si 2p XPS spectra for the SRON films are shown in Fig. 1a–e. The Si 2p peak for all the samples was deconvoluted into multiple peaks. SiO_xN_y samples with $x<0.96$ exhibited the presence of elemental silicon features, hence were fitted with appropriate constraints for the Si doublet and FWHM conditions. However, elemental silicon features were absent in $SiO_{0.96}N_{0.27}$ sample and the Si 2p spectra exhibited a broad peak comprising several peaks. The Si 2p spectra shifted towards lower binding energies with increased Si content.

Fig. 2a–e shows the measured and fitted high-resolution N 1s XPS spectra for the SRON films. While, the N 1s peak for the $SiO_{0.96}N_{0.27}$ and $SiO_{0.49}N_{0.19}$ samples were fitted with two peaks, for rest of the samples, the N 1s spectra could be fitted with single peak. N 1s spectra also shifted towards lower binding energies with increased Si content.

Fig. 3a–e shows the experimental and modeled values of the ellipsometric data, ψ, as a function of incident angle at a fixed wavelength of 600 nm for the SRON films. Si and SiO_2 were assumed to be the constituents of this SRON layer. Mean Square Errors for the simulated curves were less than 2.0. Introduction of Si_3N_4, a possible third constituent of the SRON Effective Medium Approximation model layer, did not cause any further reduction of the mean square error values. A 500-nm SiO_2 layer was included between the SRON layer and silicon substrate for modeling purposes. The optical constants of the 500-nm SiO_2 layer were obtained separately by fitting the ellipsometric data and are also shown for comparison in Fig. 3f.

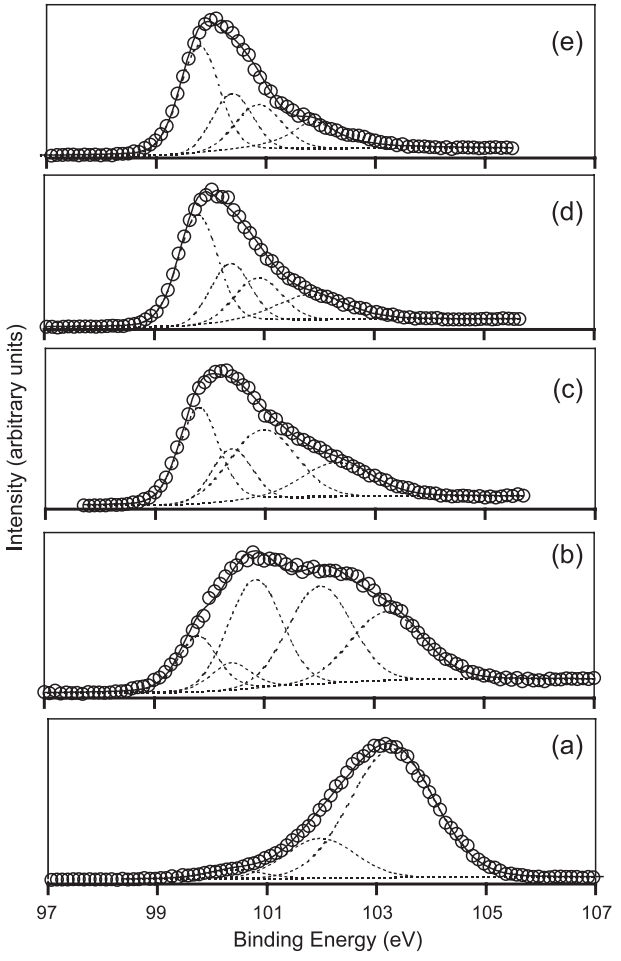

Fig. 1. Measured and fitted Si 2p spectra of the (a) $SiO_{0.96}N_{0.27}$, (b) $SiO_{0.49}N_{0.19}$, (c) $SiO_{0.29}N_{0.13}$, (d) $SiO_{0.18}N_{0.09}$ and (e) $SiO_{0.17}N_{0.07}$ films. (○) represents the measured data points, (—) fitted curve, (- -) individual peaks. Peak assignments can be found in Table 1.

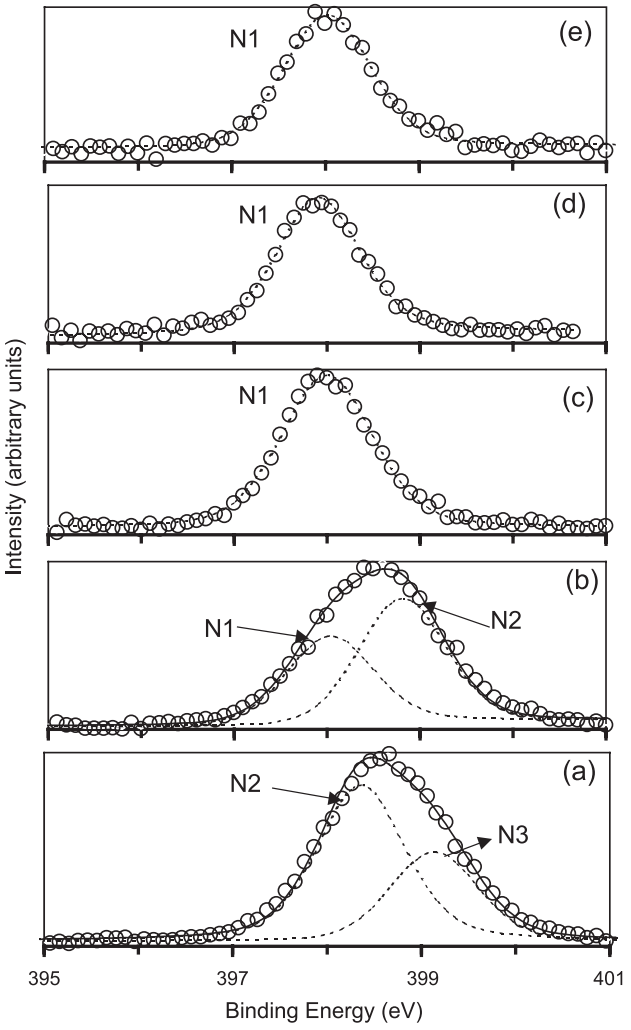

Fig. 2. Measured and fitted N 1s spectra of the (a) $SiO_{0.96}N_{0.27}$, (b) $SiO_{0.49}N_{0.19}$, (c) $SiO_{0.29}N_{0.13}$, (d) $SiO_{0.18}N_{0.09}$ and (e) $SiO_{0.17}N_{0.07}$ films. (○) represents the measured data points, (—) fitted curve, (- -) individual peaks. Chemical state corresponding to individual peak is shown. (N1) Si_3N_4; (N2) SiO_xN_y; (N3) N-SiH_2.

Fig. 4 shows the variation of the refractive index values of SRON films as a function of O/Si (x) and O/N (z) ratio. As seen in Fig. 4a, the refractive index of the films increased linearly from 1.61 to 2.74 as the O/Si ratio was decreased from 0.96 to 0.17. The equation for the linear dependence of refractive index on the O/Si ratio is also shown in Fig. 4a. The refractive index of films other than $SiO_{0.17}N_{0.07}$ also exhibited a linear dependence on the O/N ratio. The linear equation established for films other

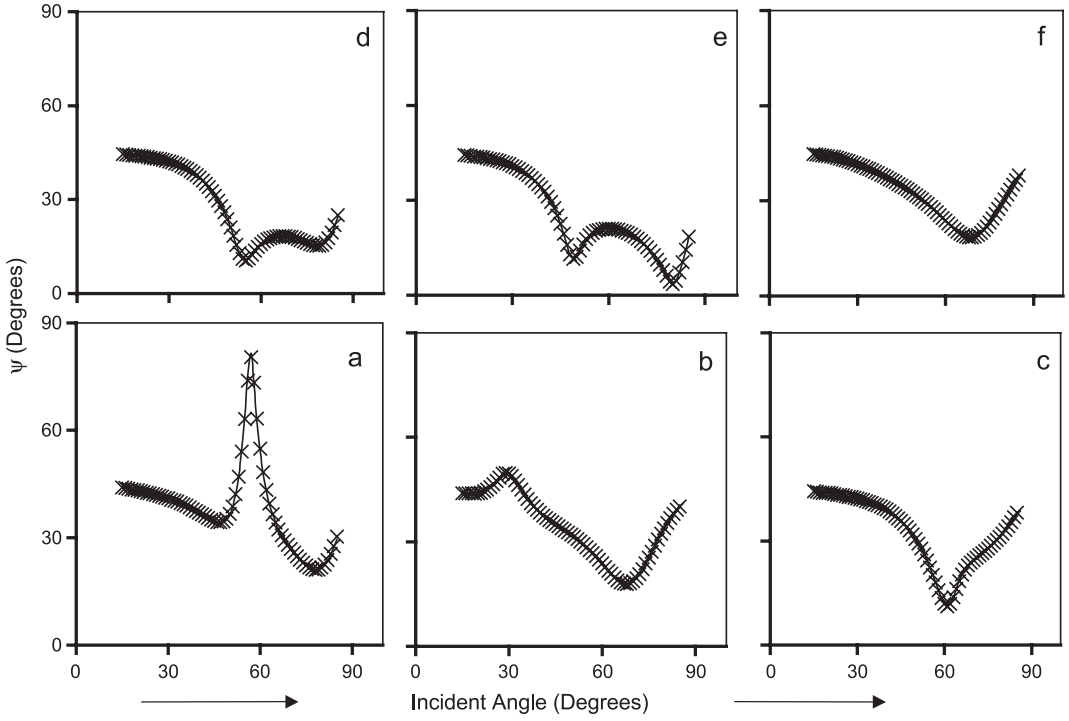

Fig. 3. Measured and fitted ellipsometry data ψ as a function of incident angle at λ=600 nm for (a) $SiO_{0.96}N_{0.27}$, (b) $SiO_{0.49}N_{0.19}$, (c) $SiO_{0.29}N_{0.13}$, (d) $SiO_{0.18}N_{0.09}$, (e) $SiO_{0.17}N_{0.07}$ and (f) 500-nm SiO_2 samples. (×) represents the measured data points and (—) the fitted curve.

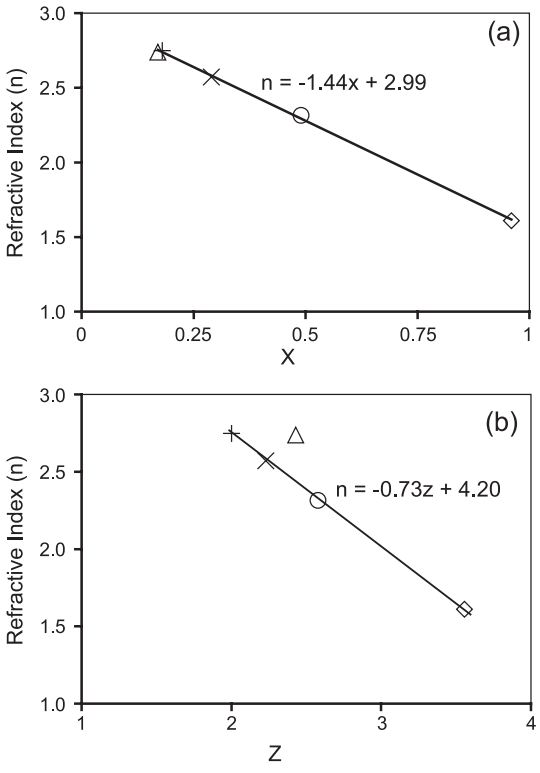

Fig. 4. Dependence of the refractive index of (◇) $SiO_{0.96}N_{0.27}$, (○) $SiO_{0.49}N_{0.19}$, (×) $SiO_{0.29}N_{0.13}$, (+) $SiO_{0.18}N_{0.09}$, (△) $SiO_{0.17}N_{0.07}$ films on (a) O/Si ratio (plotted as x) and (b) O/N ratio (plotted as z). Linear equations that fit the data points are also shown. Refractive index value for $SiO_{0.17}N_{0.07}$ film was excluded for establishing the linear equation in (b).

than $SiO_{0.17}N_{0.07}$ is also shown in Fig. 4b. The thickness of the films were determined to be 150.7, 167.4, 207.0, 276.9, 534.8 nm for $SiO_{0.17}N_{0.07}$, $SiO_{0.18}N_{0.09}$, $SiO_{0.29}N_{0.13}$, $SiO_{0.49}N_{0.19}$, $SiO_{0.96}N_{0.27}$, respectively. A linear variation in the SRON film thickness as a function of O/Si content was also observed in the films. Since the density of the bulk Si, amorphous SiO_2 and Si_3N_4 are ~2.3, 2.2, and 3.44 gm/cm^3, respectively, a variation in the density of the film could not have caused such a large variation in the thickness of the films. Therefore, we attribute this nonlinear variation in the film thickness to the deposition conditions.

FTIR absorbance spectra for SRON films are shown in Fig. 5a–e. The spectra showed the presence of a Si–H stretching peak in the range 2000–2200 cm^{-1} and a Si–O stretching peak near 1080 cm^{-1}. FTIR absorbance spectra were deconvoluted into multiple overlapping peaks using GRAMS-AI software [16]. As seen in Fig. 5a, a Si_3N_4 peak around 850 cm^{-1} and Si–O stretching peaks were distinguishable for films with x=0.96. However, an increase in the silicon content of the films (Fig. 5b–e) caused these peaks to shift towards lower energy and a strong overlap between the individual peaks was observed in the fitted curves. While the Si–O stretching peak in SiO_x films can decrease from 1075 to 965 cm^{-1} with decreasing oxygen content [17], it has been observed that in the FTIR spectra of SiO_xN_y films, the dominant single phase Si–O/Si–N stretching vibration maxima varied from 850 to 1072 cm^{-1} for $0.26 \leq x \leq 2.0$ and $1.2 \geq y \geq 0$ [18]. The qualitative and quantitative analyses of

the Si–O stretching peak were made difficult by the above observations, as well as the variation of the film thicknesses, hence were not attempted.

Fig. 6a–e shows the room temperature normalized PL spectra of the SRON films. The luminescence spectra consisted a series of broad peaks and were deconvoluted into high-energy (HE) and low-energy (LE) components. The luminescence spectra shifted towards lower energies with increasing silicon content. Although, the HE component in $SiO_{0.18}N_{0.09}$, $SiO_{0.17}N_{0.07}$ films did not have a good signal to the noise ratio, it could clearly be seen as a high-energy shoulder in the respective spectra (Fig. 6d and e). Fig. 7 shows the dependence of the HE and LE luminescence components on the O/Si (x) and O/N (z) ratios. As seen in Fig. 7a, the positions of HE and LE luminescence peaks remained constant when the O/Si ratio was varied from 0.96 to 0.49. With further decrease of the O/Si to 0.29 the HE and LE components shifted towards lower energies. However, with further decrease in the O/Si to 0.18, the HE and LE peaks shifts towards higher energies. Similar values of HE and LE peak energies were found for samples with O/Si ratio 0.18 and O.17. The low signal to the noise ratio of HE component, hence the inaccuracy in the determination of the peak position of this component, could be one of the reason for the shift of the HE components to higher energy values. However, the significant shift of the LE component values towards higher energies for the samples with O/Si ratio 0.18 and 0.17 was reliable.

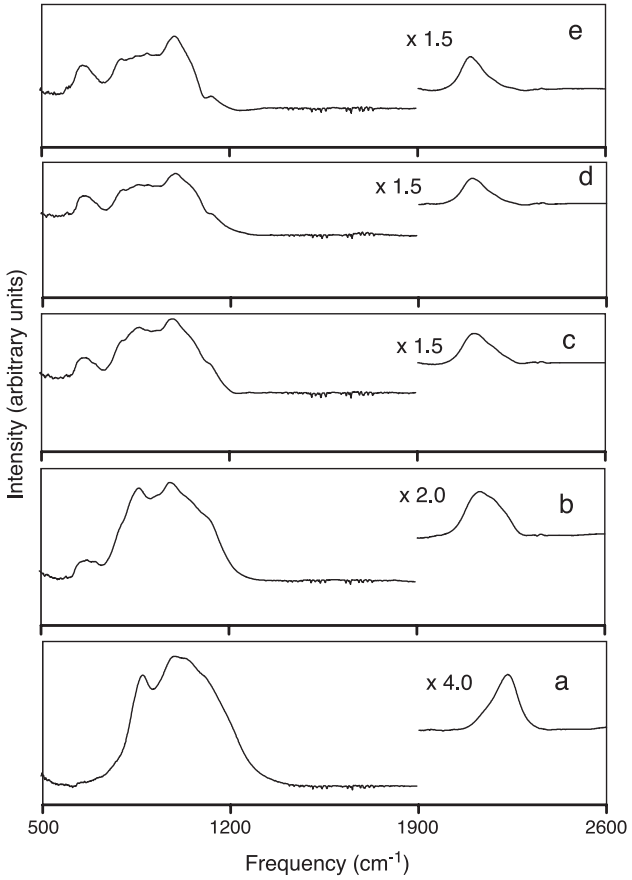

Fig. 5. FTIR absorbance spectra of (a) $SiO_{0.96}N_{0.27}$, (b) $SiO_{0.49}N_{0.19}$, (c) $SiO_{0.29}N_{0.13}$, (d) $SiO_{0.18}N_{0.09}$ and (e) $SiO_{0.17}N_{0.07}$. The spectra in the range 1900–2600 cm^{-1} have been multiplied by an appropriate factor to elucidate the Si–H stretching band.

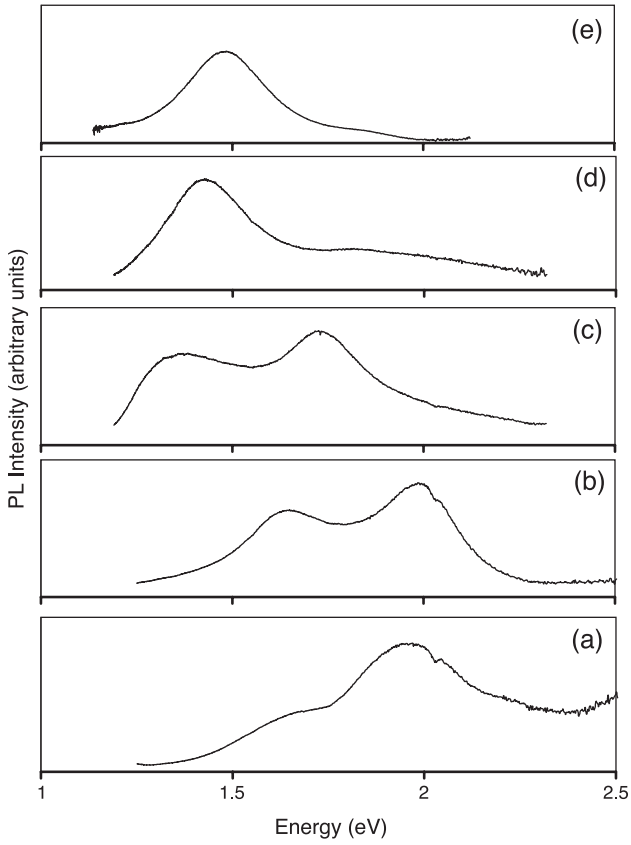

Fig. 6. Normalized room-temperature photoluminescence spectra of (a) $SiO_{0.96}N_{0.27}$, (b) $SiO_{0.49}N_{0.19}$, (c) $SiO_{0.29}N_{0.13}$, (d) $SiO_{0.18}N_{0.09}$ and (e) $SiO_{0.17}N_{0.07}$ films.

In order to explore the dependence of HE and LE peak positions on the O/N ratio, the HE and LE components were plotted as a function of the O/N ratio (Fig. 7b). As seen in the figure, the energy positions of HE and LE luminescence peaks remained constant when the O/N ratio was varied from 3.6 to 2.6. Further decrease of the O/N to 2.4 caused the HE and LE components to significant shift towards lower energies. This decreasing trend continued as the O/N ratio was further decreased to 2.2. However, with further decreases of the O/N ratio to 2.0 the HE and LE component shifted back towards higher energies. The argument for the uncertainties in the HE component used in the previous paragraph is also valid here.

4. Discussion

Our as-deposited, amorphous SiO_xN_y/H films comprised silicon, oxygen, nitrogen and bonded hydrogen, based on XPS elemental analysis and IR spectroscopy. These SRON

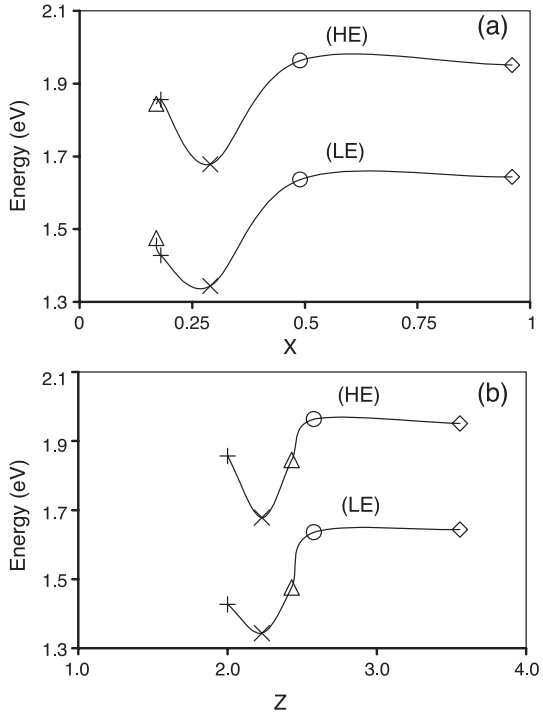

Fig. 7. Dependence of the high-energy (HE) and low-energy (LE) luminescent peak position of (◇) $SiO_{0.96}N_{0.27}$, (○) $SiO_{0.49}N_{0.19}$, (×) $SiO_{0.29}N_{0.13}$, (+) $SiO_{0.18}N_{0.09}$, (△) $SiO_{0.17}N_{0.07}$ films on (a) O/Si ratio (plotted as x) and (b) O/N ratio (plotted as z).

films have been deposited by varying the ratio of the SiH_4/N_2O reactant precursors. Increasing the silane concentration caused x to decrease from 0.96 to 0.18. However, further increases in silane concentration could not be utilized to decrease x to values lower than 0.17; thus, elucidating the limiting behavior of the deposition process. Since nitrogen was introduced to the film as N_2O, it was likely that the films with lower silicon content or larger oxygen content would have concomitant increased nitrogen content. This assumption is consistent with the survey XPS data for our SRON films.

The binding energy for elemental silicon is ~99.8eV and that of fully oxidized SiO_2 (Si^{4+}) is ~103.5 eV. The binding energies of intermediate Si oxidation states (Si^{1+}, Si^{2+}, Si^{3+}) are found between these values. The energy shift per Si–O bond is usually constant [13]. The Si2p peaks for silicon nitride are found around 101.8±0.4 eV [19,20]. However, depending on the nitrogen content, the peaks for SiO_xN_y are known to vary between the peak positions for SiO_2 and Si_3N_4 [21,22]. Based on these reports, the chemical state assignments of Si2p XPS peaks for our samples are also shown in Table 1. The $SiO_{0.96}N_{0.27}$ sample was a complicated mixture of silicon oxide, sub-oxide, and oxynitride phases. Elemental silicon features were present only in the SiO_xN_y samples with x<0.96. As seen in Fig. 1, the relative area of the elemental silicon peak increased with increasing silicon composition for sample with x<0.96, confirming an increased level of elemental silicon in the films with increased silicon content.

In the N 1s spectra, the binding energy for Si–N bonds in Si_3N_4 typically lies in the range 397.5–397.99 eV [21,23]. Saoudi et al. [24] had found the N 1s peak in silicon oxynitride films to vary from 398 to 398.5 as the O/N ratio was varied from 1.75 to 12.5. For nitrided Si surfaces, the N 1s peak shifted towards higher energies by 1.1–1.2 eV with respect to Si_3N_4 had been attributed to a bonding configuration of N-SiH_2.[25] Similarly, the N 1s peak shifted towards higher energies by 1.6–1.9 eV with respect to Si_3N_4 had been attributed to a bonding configuration of N-Si_2O [26]. Peaks in the range 398–399 eV had also been attributed to nitrogen bound to otherwise fully oxidized silicon [19,21]. The chemical states based on the N 1s XPS peaks for our samples are shown in Fig. 2. Hence, while the N 1s peak for silicon oxynitride phase existed for our $SiO_{0.96}N_{0.27}$ sample, $SiO_{0.49}N_{0.19}$ had a mixture of silicon nitride and silicon oxynitride phases. Only the N 1s peak for the silicon nitride phase was present for rest of the samples.

The equation for the linear dependence of the refractive index of the films on the O/Si and N/Si ratio was established. The linear equation for the dependence of the refractive index on the O/Si ratio (Fig. 4a) indicates that the refractive index decreases linearly from 1.61 to 2.74 as the O/Si ratio was decreased from 0.96 to 0.17. For the limiting case of O/Si ratio of 0, based on equation in Fig. 4a, the refractive index of the film should be ~3.0. This value is a reasonable number, since the refractive index of crystalline silicon at 600 nm is typically around 3.94. As seen in Fig. 4b, the refractive index also decreases linearly from 1.61 to 2.74 as the O/N ratio was decreased from 3.6 to 2.0. For the limiting case of O/N ratio of 0, the refractive index of the

Table 1
Chemical state identification Si 2p deconvoluted peaks for SiO_xN_y/H samples

SiO_xN_y	Binding energy (eV)	Possible chemical states
$SiO_{0.96}N_{0.27}$	100.4	Si^{1+}
	102.0	Si^{2+}; SiO_xN_y
	103.3	Si^{4+}
$SiO_{0.49}N_{0.19}$	99.8	Si $2p_{3/2}$
	100.4	Si $2p_{1/2}$
	100.8	Si^{1+}
	102.0	Si^{2+}; SiO_xN_y; Si_3N_4
	103.2	Si^{4+}
$SiO_{0.29}N_{0.13}$	99.8	Si $2p_{3/2}$
	100.4	Si $2p_{1/2}$
	101	Si^{1+}
	102.3	Si_3N_4; Si^{2+}
$SiO_{0.18}N_{0.09}$	99.8	Si $2p_{3/2}$
	100.4	Si $2p_{1/2}$
	100.9	Si^{1+}
	101.9	Si_3N_4
$SiO_{0.17}N_{0.07}$	99.8	Si $2p_{3/2}$
	100.4	Si $2p_{1/2}$
	100.9	Si^{1+}
	101.9	Si_3N_4

film based on equation in Fig. 4b should be ~4.2. This value is clearly not a reasonable number based on the fact that the refractive index of silicon nitride at 600 nm is typically around 2.02. Therefore, based on these arguments, while the linear dependence of the refractive index on O/Si had both mathematical and physical significance, the dependence of refractive index on the O/N ratio was not reasonably established.

In the FTIR spectra of the films with x<0.96, the shift of silicon-nitride and Si–O stretching peaks towards lower energies was possibly due to the increased nitride character and oxygen deficiency in these films, as compared to the film with x=0.96. The presence of an absorbance peak in the range 2000–2200 cm^{-1} indicates the presence of hydrogen bonded to silicon in all the films. It has been shown in the past that the frequency of the Si–H stretching bond in amorphous solids is dependent upon the nearest neighboring atoms (A_j) and can be expressed as [27]

$$v_{\mathrm{Si-H}} = 1740.7 + 34.7 \sum_{j=1}^{3} \mathrm{SA}(A_j) \quad (1)$$

where SA(A_j) is the Sanderson electronegativity and is related to the Pauling electronegativity ($X(A_j)$) by

$$\left[X(A_j)\right]^{1/2} = 0.21\mathrm{SR}(A_j) + 0.77 \quad (2)$$

The uncertainty in the frequency of the Si–H stretching peak for a given SR sum was estimated to be 12.8 cm^{-1}. Luckovsky [27] postulated the following equation describing the cubic dependence of the Si–H bond distance ($d_{\mathrm{Si-H}}$) on the frequency of the Si–H ($v_{\mathrm{Si-H}}$) stretching peak

$$v_{\mathrm{Si-H}}\left(d_{\mathrm{Si-H}}\right)^3 = 7074\ \mathrm{cm}^2 \quad (3)$$

Table 2 lists the peak frequencies and relative intensities of fitted Si–H peaks for our different samples. Based on Eqs. (1) and (2), the calculated peak frequency and nearest neighboring atoms are also presented in the table. Table 2 also lists the values of the Si–H bond distances calculated using Eq. (3). The Si–H bond distances ($d_{\mathrm{Si-H}}$) for Si–H in a-Si and a-SiO_2 were calculated to be ~1.52 and ~1.44 Å [27], with the $d_{\mathrm{Si-H}}$ for various substituted silane molecules lying between these two values along a line connecting them. In our samples, the fitted Si–H stretching peaks comprised several individual components; therefore, the weighted average of the $d_{\mathrm{Si-H}}$ ($W_{d_{\mathrm{Si-H}}}$) was used as a marker to ascertain the compositional dependence of the Si–H bond distance. As seen in the table, the weighted Si–H bond distance increased from 1.47 to 1.49 Å as x decreased from 0.96 to 0.29. Further decreases in the value of x did not cause any further changes in the weighted Si–H bond distance. The observed increase in the Si–H bond distance could be attributed to the increased silicon content in the film, which led to an increase in the number of silicon atom neighbors to the Si–H species.

All the as-deposited films exhibit room temperature luminescence. PL spectra of the films were resolved into HE and LE components. As seen in Fig. 7, the position of the HE and LE peaks displayed a systematic, nonlinear dependence on both O/Si and O/N ratio for all the samples except $SiO_{0.18}N_{0.09}$. Augustine et al. [5] had attributed the

Table 2
Experimental and calculated peak position of Si–H stretching bond and their corresponding nearest-neighbors for SiO_xN_y/H samples

	Relative intensity	Experimental peak position (cm^{-1})	Calculated peak position (cm^{-1})	Nearest neighboring atoms			$d_{\mathrm{Si-H}}$ (Å)	$W_{(d_{\mathrm{Si-H}})}$ (Å)
				1	2	3		
$SiO_{0.96}N_{0.27}$	35	2238	2242	O	N	N	1.46	1.47
	100	2207	2200	O	O	Si	1.47	
$SiO_{0.49}N_{0.19}$	16	2238	2242	O	N	N	1.46	1.48
	16	2195	2199	O	N	H	1.47	
	100	2130	2138	O	Si	H	1.49	
$SiO_{0.29}N_{0.13}$	6	2239	2242	O	N	N	1.46	1.49
	50	2178	2181	O	N	Si	1.48	
	5	2139	2138	O	Si	H	1.48	
	100	2103	2103	N	Si	Si	1.49	
	6	2032	2042	Si	Si	Si	1.51	
$SiO_{0.18}N_{0.09}$	7	2231	2242	O	N	N	1.46	1.49
	4	2189	2181	O	N	Si	1.47	
	100	2112	2103	N	Si	Si	1.49	
	9	2090	2103	H	H	Si	1.50	
$SiO_{0.17}N_{0.07}$	5	2249	2242	O	N	N	1.46	1.49
	52	2162	2163	N	N	Si	1.48	
	5	2135	2138	O	Si	H	1.48	
	100	2093	2103	N	Si	Si	1.49	
	14	2034	2042	Si	Si	Si	1.51	

The Si–H bond distance is also listed.

room temperature PL in their SiO_xN_y/H samples due to the defects in the silicon-suboxide moiety. Recently, on the basis of their Raman and PL studies, Ribeiro et al. [7] had attributed variable-sized amorphous silicon clusters embedded in the dielectric matrix to be responsible for room the temperature PL in the range 1.5–2.0 eV. We attribute the presence of embedded amorphous silicon clusters to be the origin of the tunable visible PL at room temperature in our samples. This assumption is based on XPS results where we could clearly see the presence of elemental silicon features in most of our samples. The similar values of HE and LE PL peak maxima were observed for $SiO_{0.96}N_{0.27}$ and $SiO_{0.49}N_{0.19}$ samples. This is possibly due to increased volume fraction of embedded amorphous silicon clusters in $SiO_{0.49}N_{0.19}$ samples with size similar to those of clusters in $SiO_{0.96}N_{0.27}$ sample. With a further decrease in the O/Si and O/N ratios, the cluster size increased leading to the red shift of the PL peak maxima. The O/N ratio played an important role in defining cluster diameters and consequently the PL peak maximum components for samples with O/Si ratios lower than 0.49. The presence of more than a single PL peak is indicative of the presence of two different average cluster diameters in these films. The reasons for the increase in the energy values of the LE peak for sample with O/Si ratio 0.18 and O/N ratio of 2.0 ($SiO_{0.18}N_{0.09}$) are not clear. It is likely that at this composition, the material exhibits some transformation in its structural and luminescence properties. One explanation could be that at this O/N ratio, the material transforms from silicon rich oxynitride to a-Si/H film with oxygen and nitrogen impurities. This seems to be a plausible scenario based on the fact that the luminescence spectra of a-Si/H typically comprise a broad luminescence maximum in the range 1.3–1.4 eV that can be tuned into the visible spectral region by varying the alloy composition of the film [5]. However, more luminescence studies involving room temperature and low-temperature luminescent spectroscopy are needed to understand this behavior.

5. Conclusions

Chemical, optical, vibrational and properties of silicon rich oxynitride films, SiO_xN_y with $0.17 \le x \le 0.96$ and $0.07 \le y \le 0.27$, have been investigated. XPS has been used to probe the chemical composition and chemical states of the constituents. Elemental silicon features appeared in the Si 2p spectra of the SiO_xN_y films with $x<0.96$. The Si 2p and N 1s spectra shifted towards lower binding energy with increased silicon content. The SiO_xN_y samples with $x<0.96$ exhibited increased elemental silicon character with increased silicon content. Based on its N 1s spectra, $SiO_{0.96}N_{0.27}$ had nitrogen primarily in the silicon-oxynitride phase. However, nitrogen was bound to a mixture of silicon nitride and silicon oxynitride phases for $SiO_{0.49}N_{0.19}$. Nitrogen was bound only in the silicon nitride phase for rest of the samples. The refractive index of the SRON films decreases linearly from 1.61 to 2.74 as the O/Si ratio was decreased from 0.96 to 0.17. The chemical environment around Si–H bonds was identified based on the stretching frequency of Si–H bond. The Si–H bond distance for the SRON sample with $x=0.96$ was found to be 1.47 Å and this increased to 1.49 Å for samples with $0.17 \le x \le 0.29$. The increased silicon content in the film, which led to an increase in the silicon neighbors around Si–H, caused this increase in Si–H bond length. The photoluminescence spectra of the SRON films attributed to embedded amorphous silicon clusters. The presence of more than a single luminescence peak was attributed to two different average sizes of the embedded clusters. Finally, we postulated that at this O/N ratio the film underwent a transformation from silicon-rich oxynitride to a-Si/H film with oxygen and nitrogen impurities.

Acknowledgements

Authors are grateful to Dr. Vincent B. Crist for valuable suggestions and help with the analysis of the XPS data. Acknowledgements are due to Dr. Patrick R. McCurdy for assistance with XPS data acquisition. Financial support provided by the NSF instrument Grant Nos. NSF-CHE-9808024 and NSF-DMR-0076180 is also acknowledged.

References

[1] M.L. Green, E.P. Gusev, R. Degraeve, E.L. Garfunkel, J. Appl. Phys. 90 (2001) 2057.
[2] K. Worhoff, L.T.H. Hilderink, A. Driessen, P.V. Lambeck, J. Electrochem. Soc. 149 (2002) F85.
[3] E. Desbiens, R. Dolbec, M.A. El Khakani, J. Vac. Sci. Technol., A 20 (2002) 1157.
[4] D.A. Buchanan, IBM J. Res. Develop. 43 (1999) 245.
[5] B.H. Augustine, E.A. Irene, Y.J. He, K.J. Price, L.E. McNeil, K.N. Christensen, D.M. Maher, J. Appl. Phys. 78 (1995) 4020.
[6] H. Kato, A. Masuzawa, H. Sato, T. Noma, K.S. Seol, M. Fujimaki, Y. Ohki, J. Appl. Phys. 90 (2001) 2216.
[7] M. Ribeiro, I. Pereyra, M.I. Alayo, Thin Solid Films 426 (2003) 200.
[8] J.A. Theil, G.A. Kooi, and R.P. Varghese, Europe Patent No. 1164206, 2001.
[9] M. Schuster, H. Göebel, J. Phys., D, Appl. Phys. 28 (1995) A270.
[10] D.J. Nagel, J.V. Gilfrich, T.W. Barbee, Nucl. Instrum. Methods 195 (1982) 63.
[11] J.F. Moulder, W.F. Stickle, P.E. Sobol, K.D. Bomben, W.F. Stickle, P.E. Sobol, K.D. Bomben, Handbook of X-ray Photoelectron Spectroscopy—A Reference Book of Standard Spectra for Identification and Interpretation of XPS Data, Physical Electronics, Eden Prairie, MN, 1995.
[12] B.V. Crist, Handbook of Monochromatic XPS Spectra Semiconductors, John Wiley & Sons, West Sussex, England, 2000, p. 356.
[13] F. Rochet, G. Dufour, H. Roulet, B. Pelloie, J. Perriere, E. Fogarassy, A. Slaoui, M. Froment, Phys. Rev., B Condens. Matter 37 (1988) 6468.
[14] S. Kohli, J.A. Theil, R.D. Snyder, C.D. Rithner, P.K. Dorhout, J. Vac. Sci. Technol., B 21 (2003) 719.
[15] Guide to using WVASE32™ J.A. Woolam Co.

[16] 7.01, Thermo Galactic (1991–2002).
[17] B.J. Hinds, F. Wang, D.M. Wolfe, C.L. Hinkle, G. Lucovsky, J. Non-Cryst. Solids 227–230 (1998) 507.
[18] A. del Prado, I. Martil, M. Fernandez, G. Gonzalez-Diaz, Thin Solid Films 343–344 (1999) 437.
[19] D. Bouvet, P.A. Clivaz, M. Dutoit, C. Coluzza, J. Almeida, G. Margaritondo, F. Pio, J. Appl. Phys. 79 (1996) 7114.
[20] G.M. Ingo, N. Zacchetti, D. Dellasala, C. Coluzza, J. Vac. Sci. Technol., A 7 (1989) 3048.
[21] M.H. Cho, Y.S. Roh, C.N. Whang, K. Jeong, D.H. Ko, J.Y. Yoo, N.I. Lee, K. Fujihara, J. Vac. Sci. Technol., A 20 (2002) 1676.
[22] R. Saoudi, G. Hollinger, A. Gagnaire, M. Pitaval, P. Molle, J. Phys., IV 5 (1995) 557.
[23] C.H.F. Peden, J.W. Rogers, N.D. Shinn, K.B. Kidd, K.L. Tsang, Phys. Rev., B 47 (1993) 15622.
[24] R. Saoudi, G. Hollinger, A. Gagnaire, M. Pitaval, P. Molle, J. Phys., III 5 (1995) 557.
[25] G.M. Rignanese, A. Pasquarello, Phys. Rev., B 63 (2001) 75307.
[26] J.P. Chang, M.L. Green, V.M. Donnelly, R.L. Opila, J. Eng, J. Sapjeta, P.J. Silverman, B. Weir, H.C. Lu, T. Gustafsson, E. Garfunkel, J. Appl. Phys. 87 (2000) 4449.
[27] G. Lucovsky, Solid State Commun. 29 (1979) 571.